Meccanica
https://doi.org/10.1007/s11012-022-01482-z

Tunable dissipation in elastic metamaterials via methodic reconfiguration of inertant mechanical networks

A. Aladwani · A. Mohammed · M. Nouh

Received: 30 April 2021 / Accepted: 13 January 2022

Abstract Elastic metamaterials have proposed transformative solutions to applications in structural mechanics owing to their unique capabilities in the domain of wave propagation and control. Notable among them are *inertant metamaterials* which augment their locally resonant mechanism with mechanical inerters, thereby expanding their dispersion profiles and versatility. In this work, we provide a comprehensive analysis of the different ways such profiles can be shaped via an informed reconfiguration of a hierarchical mechanical network comprising the inerter element. Through a series of examples, we demonstrate the pivotal roles played by the network components, architecture, as well as damping placement on the response, bandgap characteristics, and emergent dissipation. Using the finite element method, band structures are computed for locally resonant flexural beams with six inertant networks representative of the design spectrum, via a free wave propagation approach, i.e., waves that are not driven at a given frequency. Predictions of the infinite medium reveal that each configuration is associated with its own dissipative characteristics which are depicted using a set of unique wavenumber-free band structures directly relating Bloch damping ratios to oscillatory damped frequencies. We show that the implemented framework enables a direct comparison with the finite metamaterial counterparts via modal damping ratios obtained at discrete frequencies, providing a straightforward yet firm validation of the resultant behavior across the entire frequency spectrum. Depending on the frequency range of interest, the choice of the inertant network combined with appropriate damping deployment within the host structure or the resonating substructure can be tailored to instigate an efficient damped response which is best suited for a given application. The presented work provides a new perspective on elastic metamaterials with inertant networks, elucidating the interplay between prescribed damping and emergent dissipation and changing the current paradigm from one that merely looks at damping amount to a cost-effective, placement-based strategy which maximizes the aggregate dissipation corresponding to a given amount of damping material.

Keywords Elastic metamaterial · Bandgap · Inerter · Metadamping

---

A. Aladwani (✉)
Department of Manufacturing Engineering Technology, College of Technological Studies, 700654 Shuwaikh, Kuwait
e-mail: ae.aladwani@paaet.edu.kw

A. Mohammed
Department of Mechanical Engineering, Kuwait University, 13060 Kuwait City, Kuwait

M. Nouh
Department of Mechanical and Aerospace Engineering, University at Buffalo (SUNY), Buffalo, NY 14260, USA
e-mail: mnouh@buffalo.edu

1 Introduction

Traditional measures of active and passive vibration control are widely adopted and often effective in broadband mitigation of high-amplitude structural loads, undesirable noise, as well as seismic impacts [1, 2]. Nonetheless, the continuous need of an electrical input in active techniques and the low strength and load-carrying ability associated with passive viscous or viscoelastic materials pose serious questions about the practicality of these measures. As a result, elastic metamaterials have recently jumped to the forefront of creative solutions which, owing to their unique wave dispersive mechanics, can provide targeted suppression of incident excitations through resonant scattering in an elastic medium [3–9]. In their most common form, elastic metamaterials comprise a host structure which either houses or is attached to an array of periodic local resonators. The ability of such array to confine and manipulate incident waves was first demonstrated by Liu et al. [10] in fabricated sonic crystals, giving rise to narrow frequency bandgaps which open up at a subwavelength scale and can be potentially tuned to low frequency regimes without large size trade-offs. The idea has since rapidly spread to a wide range of structures with variations of the same concept adopted in a large portfolio of mechanical configurations and platforms. Examples range from lattices to solid continua [11, 12], bars to flexural beams [13, 14], one-dimensional to multi-dimensional and multilayered structures [15–17], as well as structures with electroelastic [18, 19] and artificially-synthesized resonant bandgaps [20].

Local resonators are classically fabricated using single or multiple degree of freedom (DOF) vibration absorbers. Although efficient in creating subwavelength bandgaps within the dispersion spectrum, the use of classical resonators have also exposed some limitations of locally resonant metamaterials. These include the narrow frequency span of induced gaps, the recurring need for large masses to tune these gaps, and the limited number of design variables with which such tunability can take place. The previous issues, as well as other, have underscored the need for novel and smart mechanisms that provide a pathway for performance enhancement of locally resonant metamaterials. Remarkable among them is the concept of inertial amplification from small masses, which was introduced by Yilmaz et al. [21] as a novel mechanism to induce bandgaps. Contrary to traditional local resonance and Bragg scattering phenomena which are more common in literature, such mechanism has been successfully used to produce wide and low frequency bandgaps in one, two, and three dimensional periodic structures [22–26]. Inspired by this concept, a class of elastic metamaterials, typically referred to as “inertant metamaterials” (IMMs), has recently gained traction owing to its demonstrable superior dispersion properties. In their design, IMMs exploit the mechanical inerter as a source of inertial amplification, by replacing classical resonators that are used in conventional metamaterials with inerter-based resonators, henceforth referred to as “inerter resonators”. In this framework, inerters can be perceived as discrete elements which constitute the ideal inertial equivalent of springs and dampers, providing a force that is proportional to the relative acceleration between two terminals. The mechanical inerter concept was originally introduced by Smith [27] in an analogy with electrical networks. It was first synthesized by meshing a flywheel with a rack gear, with the flywheel’s pivot forming one terminal of the device and the rack gear forming the other [28]. Shortly thereafter, the principle was used in suspension systems of racing cars under the alternative name of the *J-damper* and has since been implemented in various forms in studies pertaining to vibration absorption [29–32]. In the context of bandgap materials and structures, the mechanical inerter was recently integrated in lumped parameter metamaterials [33, 34], continuous metastructures [35–37], as well as tunable metasurfaces [38]. Most recently, novel configurations of IMMs have been shown to enhance seismic base isolation properties [39], and induce double attenuation peaks within low frequency bandgaps while retaining decent bandgap strength [40].

Despite their promise, studies of IMMs although valiant efforts, have undertaken either a simple swap of a spring-mass absorber with an inerter element or mostly focused on a limited number of design configurations. As will be shown throughout this work, the precise placement of the inerter within the locally resonant mechanical network and the architecture of the network itself play a profound role in the resultant behavior which can be tailored to serve varying needs. Furthermore, efforts pertaining to the (1) effect of, and (2) source of damping in inertant metamaterials have been scarce, if not nonexistent. As a result, the driven wave approach has consistently been the method of choice in most (if not all) of the efforts in this domain. The study of dissipative elements in elastic metamaterials has rapidly gone beyond the mere analysis of undesirable effects in the attenuated dynamic response and has provided an intriguing avenue to remarkably amplify the metamaterial's spatial and temporal dissipative capacity over a frequency range of interest; a concept typically referred to as metadamping in locally resonant structures [41]. The favorable implications of metadamping have recently been quantitatively and qualitatively illustrated across a sweeping range of bandgap systems including viscoelastic [42], mono/bi-polar and non-local [43, 44], flexural [45], as well as multi-resonator [46] metamaterials. As such, the absence of a comprehensive examination of the possible functionalities provided by dissipative IMMs with viscously damped inerter-based resonators represents missed opportunity and an untapped design resource which will be a central focus of this work.

In this paper, the wave dispersion patterns of IMMs are investigated using the finite element method (FEM) for six different design configurations. Each of these configurations is associated with its own bandgap characteristics, which are interpreted as function of the: (1) inertance ratio and (2) frequency ratio, which are non-dimensional parameters. By implementing a free wave approach, the damping ratio band structure emerges as a unique feature that provides a platform for analyzing the metadamping phenomenon which would otherwise be impossible to address using the commonly used driven wave approach. Upon the conclusion of this effort, it will become evident that IMMs can be used to achieve dissipative characteristics that utterly depart from conventional metamaterials. The paper is organized as follows: following the introduction and a brief outline of the inertant metamaterial beam configurations, the computational free wave framework is presented in light of the different unit cell motion equations. Following which, we detail the different aspects pertaining to bandgap formation in undamped IMMs. The focus is then shifted to the damped IMM configurations and damping is applied separately at the host structure, the non-inerter component of the resonant inclusion, and finally within the inerter-containing network of the resonator.

2 Computational free wave dispersion mechanics

2.1 Inertant metamaterial beam configurations

An inerter is a two-terminal mechanical element (see Fig. 1) that operates on the relative acceleration of its terminals such that

$$F_i = b(\ddot{u}_2 - \ddot{u}_1) \tag{1}$$

where F_i is the force exerted in the inerter element, b is the inertance, and $\ddot{u}_1$ and $\ddot{u}_2$ are the accelerations defined at terminals 1 and 2, respectively. There are many ways in which an inerter can be incorporated into a resonator. In this article, inerter resonators comprised of different mechanical networks are utilized in place of classical resonators in locally resonant metamaterial beams in order to investigate their vibration and wave propagation characteristics. Henceforth, we refer to this class of metamaterials as *inertant metamaterials*. Figure 2a shows a schematic diagram of a cantilevered inertant metamaterial beam where a set of periodic lumped masses are attached to the lower surface of the host beam. As shown in Fig. 2b, each lumped mass is connected to the host beam via a spring k_v, a viscous damper c_v, and a mechanical network (MN) which comprises an inerter b as one of its components. Figure 2c displays some of the most commonly used mechanical network configurations in inerter-based dynamic vibration absorbers [47], which will be individually investigated here when embedded as part of a periodic self-repeated local resonator unit cell. k_i and c_i represent the mechanical network's spring and viscous damper, respectively. To fully understand the working mechanics of inertant metamaterials, a number of undamped configurations: UC1, UC2, and UC3 will be analyzed first, followed by the damped configurations: DC1, DC2, and DC3. It should be noted that the undamped configurations UC2 and UC3 can be obtained by setting $c_i = 0$ in DC2 and DC3, respectively, and can therefore be thought of as their corresponding counterparts. The

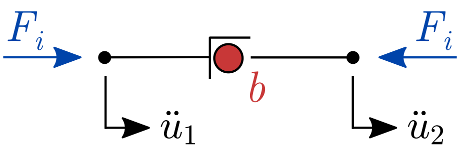

Fig. 1 Schematic of a mechanical inerter

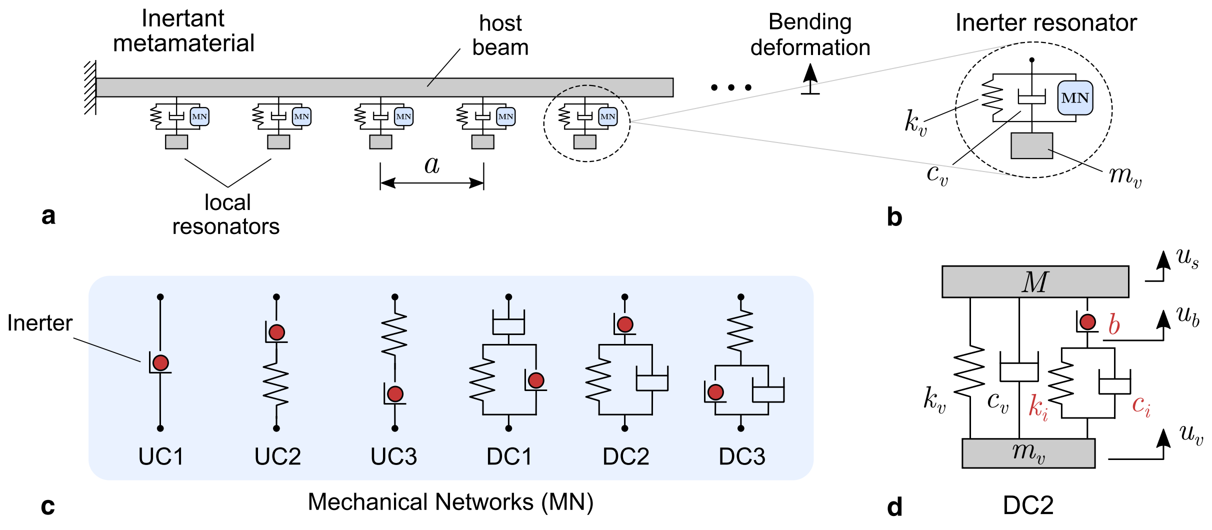

Fig. 2 Inertant metamaterials. Schematic diagrams of **a** A cantilevered inertant metamaterial beam and **b** an inerter resonator comprised of a lumped mass suspended from a spring and a viscous damper, both in parallel with a mechanical network (blue box). The six mechanical networks studied here are shown in **c**. **d** A discrete model of an inertant unit cell comprising a primary mass and an inerter resonator with DC2 as the mechanical network. (Color figure online)

analysis of the three leftmost configurations in Fig. 2c via a free wave approach will give insight into the bandgap characteristics of inertant metamaterials in their non-dissipative form. Following which, damping effects will be detailed via a thorough examination of the three rightmost networks, which will shed light on some of the important features associated with damped resonant inclusions in elastic metamaterials (i.e., the metadamping phenomenon) in the presence of inerter elements.

In the following three subsections, a generalized computational framework is developed based on the FEM to compute band structures of inertant metamaterials. To ensure a systematic process, the framework is divided into the following three steps: (1) In the first step, the finite element equations of motion (EOMs) are obtained for a generic unit cell. This is followed by the application of Bloch periodicity boundary conditions, leading to a wavenumber-dependent eigenvalue problem that can be solved for complex frequencies, from which band structures can be obtained. (2) In the second step, the EOMs corresponding to the mechanical network configurations shown in Fig. 2c are derived using simplified lumped parameter models, and (3) In the third step, we show how to integrate steps 1 and 2 in a generalized finite element context.

2.2 FEM-based free wave solution

Consider a free unit cell representing an infinitely periodic metamaterial beam with a displacement field denoted by the vector $\mathbf{u}$. Employing Bloch's theorem, the wave field vector can be expressed as $\mathbf{u}(x,\kappa,t)=\tilde{\mathbf{u}}(x,\kappa)e^{j\kappa x+\lambda t}$, satisfying the periodicity constraint given by $\tilde{\mathbf{u}}(x,\kappa,t)=\tilde{\mathbf{u}}(x+a,\kappa,t)$, where $\tilde{\mathbf{u}}$ is the periodic amplitude vector, a represents the spatial periodicity of the unit cell in the x-direction, κ is the wavenumber, and λ is a complex frequency function that permits wave attenuation in time. Applying the periodicity constraint, Bloch's theorem enables the displacement field to be expressed as a relationship between the unit cell boundaries such that

$$\mathbf{u}(x+a,\kappa,t)=\mathbf{u}(x,\kappa,t)e^{j\kappa a} \tag{2}$$

Using FEM, $\mathbf{u}$ can be discretized into generalized displacements satisfying the EOMs given by $\mathbf{M}\ddot{\mathbf{U}}+\mathbf{C}\dot{\mathbf{U}}+\mathbf{K}\mathbf{U}=\mathbf{0}$, where $\mathbf{U}$ is the free generalized displacements vector and $\mathbf{M}$, $\mathbf{C}$, and $\mathbf{K}$ denote the unit cell mass, viscous damping, and stiffness matrices, respectively. For discretized models, Eq. (2) is equivalent to a set of Bloch periodicity boundary conditions ensuring that primal assembly of the left and right interfaces of the unit cell is possible. In this context, $\mathbf{U}$ can be expressed as $\mathbf{U} = \mathbf{P}\tilde{\mathbf{U}}$, where $\tilde{\mathbf{U}}$ is the periodic generalized displacements vector which includes only internal and left boundary displacements and rotations and $\mathbf{P}$ is the Bloch periodicity matrix, expressed as follows:

$$\mathbf{P}(\kappa) = \begin{bmatrix} \mathbf{I} & \mathbf{0} \\ \mathbf{0} & \mathbf{I} \\ \mathbf{0} & \mathbf{I}e^{j\kappa a} \end{bmatrix} \tag{3}$$

with $\mathbf{I}$ and $\mathbf{0}$ being identity and null matrices of proper sizes. In terms of $\tilde{\mathbf{U}}$, the free unit cell EOMs can be reduced to $\tilde{\mathbf{M}}\ddot{\tilde{\mathbf{U}}} + \tilde{\mathbf{C}}\dot{\tilde{\mathbf{U}}} + \tilde{\mathbf{K}}\tilde{\mathbf{U}} = \mathbf{0}$, where

$$\tilde{\mathbf{M}} = \mathbf{P}^{\dagger}\mathbf{M}\mathbf{P} \tag{4a}$$

$$\tilde{\mathbf{C}} = \mathbf{P}^{\dagger}\mathbf{C}\mathbf{P} \tag{4b}$$

$$\tilde{\mathbf{K}} = \mathbf{P}^{\dagger}\mathbf{K}\mathbf{P} \tag{4c}$$

with $\mathbf{P}^{\dagger}$ being the Hermitian transpose of the Bloch periodicity matrix. As detailed in Aladwani and Nouh [46], by introducing the state vector $\tilde{\mathbf{Y}} = [\dot{\tilde{\mathbf{U}}}\tilde{\mathbf{U}}]^T$ and assuming a solution of the form $\tilde{\mathbf{Y}} = \bar{\mathbf{Y}}e^{\lambda t}$, the eigenvalue problem $[\lambda(\kappa)\tilde{\mathbf{A}}(\kappa) + \tilde{\mathbf{B}}(\kappa)]\bar{\mathbf{Y}}(\kappa) = \mathbf{0}$ is obtained in state-space format, with

$$\tilde{\mathbf{A}} = \begin{bmatrix} \mathbf{0} & \tilde{\mathbf{M}}(\kappa) \\ \tilde{\mathbf{M}}(\kappa) & \tilde{\mathbf{C}}(\kappa) \end{bmatrix} \text{ and } \tilde{\mathbf{B}} = \begin{bmatrix} -\tilde{\mathbf{M}}(\kappa) & \mathbf{0} \\ \mathbf{0} & \tilde{\mathbf{K}}(\kappa) \end{bmatrix} \tag{5}$$

which gives complex eigenvalues of the form:

$$\lambda(\kappa) = -\zeta(\kappa)\omega_u(\kappa) \pm j\omega_d(\kappa) \tag{6}$$

where ω_u is the wavenumber-dependent undamped resonant frequency. The damped frequency ω_d, and the damping ratio ζ can be expressed as follows:

$$\omega_d(\kappa) = \mathbf{Im}[\lambda(\kappa)] \text{ and } \zeta(\kappa) = -\frac{\mathbf{Re}[\lambda(\kappa)]}{|\lambda(\kappa)|} \tag{7}$$

which can be usefully combined and presented using non-traditional band structures that are free from wavenumbers, as will be shown in Sect. 4.

2.3 Equations of discretized inertant unit cells

Each configuration in Fig. 2c has its own set of EOMs. For brevity, only the equations corresponding to the damped configurations DC1, DC2, and DC3 are derived here (with the understanding that EOMs of the undamped configurations can be easily obtained from the damped ones as indicated earlier). To this end, consider Fig. 2d which depicts a discrete model of an inertant unit cell comprising a DC2 inerter resonator attached to a lumped portion of the host beam. The model consists of a resonator mass m_v which is connected to a primary mass M via a spring of stiffness k_v, a viscous damper with coefficient c_v, both in parallel with the DC2 mechanical network. The EOMs of this 3-DOF system can be expressed as follows:

$$M\ddot{u}_s = k_v(u_v - u_s) + c_v(\dot{u}_v - \dot{u}_s) + F \tag{8a}$$

$$m_v\ddot{u}_v = -k_v(u_v - u_s) - c_v(\dot{u}_v - \dot{u}_s) - F \tag{8b}$$

$$F = b(\ddot{u}_b - \ddot{u}_s) = k_i(u_v - u_b) + c_i(\dot{u}_v - \dot{u}_b) \tag{8c}$$

where k_i and c_i are given the subscript i to indicate that they are part of the inerter-based mechanical network as stated earlier. Moreover, u_s and u_v are the displacements of the primary and resonator masses, respectively, and u_b is the intermediate DOF shown in Fig. 2d. By substituting Eq. (8c) into Eqs. (8a) and (8b) and eliminating $\ddot{u}_s$ from Eq. (8c), we arrive at the following free motion equations:

$$M\ddot{u}_s + c_v\dot{u}_s - (c_v + c_i)\dot{u}_v + c_i\dot{u}_b + k_vu_s - (k_v + k_i)u_v + k_iu_b = 0 \tag{9a}$$

$$m_v\ddot{u}_v - c_v\dot{u}_s - (c_v + c_i)\dot{u}_v - c_i\dot{u}_b - k_vu_s + (k_v + k_i)u_v - k_iu_b = 0 \tag{9b}$$

$$b\ddot{u}_b - c_i\left(1 + \tfrac{b}{M}\right)\dot{u}_v + c_i\left(1 + \tfrac{b}{M}\right)\dot{u}_b + \left(\tfrac{b}{M}\right)k_vu_s - \left[\left(\tfrac{b}{M}\right)(k_v + k_i) + k_i\right]u_v + k_i\left(1 + \tfrac{b}{M}\right)u_b = 0 \tag{9c}$$

Following analogous steps, it is straightforward to show that the EOMs with DC1 and DC3 as mechanical networks can be expressed, respectively, as follows:

$$M\ddot{u}_s + (c_v + c_i)\dot{u}_s - c_v\dot{u}_v - c_i\dot{u}_b + k_vu_s - k_vu_v = 0 \tag{10a}$$

$$m_v\ddot{u}_v - (c_v + c_i)\dot{u}_s + c_v\dot{u}_v + c_i\dot{u}_b - k_vu_s + k_vu_v = 0 \tag{10b}$$

$$b\ddot{u}_b - c_i\left(1 + \tfrac{b}{m_v}\right)\dot{u}_s + c_i\left(1 + \tfrac{b}{m_v}\right)\dot{u}_b - \left(\tfrac{b}{m_v}\right)k_vu_s + \left[\left(\tfrac{b}{m_v}\right)k_v - k_i\right]u_v + k_iu_b = 0 \tag{10c}$$

and

$$M\ddot{u}_s + c_v\dot{u}_s - c_v\dot{u}_v + (k_v + k_i)u_s - k_v u_v - k_i u_b = 0 \tag{11a}$$

$$m_v\ddot{u}_v - c_v\dot{u}_s + c_v\dot{u}_v - (k_v + k_i)u_s + k_v u_v + k_i u_b = 0 \tag{11b}$$

$$b\ddot{u}_b - c_i\dot{u}_v + c_i\dot{u}_b - \left[(\tfrac{b}{m_v})(k_v + k_i) + k_i\right]u_s + \left(\tfrac{b}{m_v}\right)k_v u_v + k_i\left(1 + \tfrac{b}{m_v}\right)u_b = 0 \tag{11c}$$

2.4 Augmented finite element matrices

Because the FEM is used to compute band structures as outlined in Sect. 2.2, it is important to show how to build the finite element matrices of a given inertant metamaterial beam in a systematic manner. As a starting point, the finite element matrices of a Timoshenko host beam can be easily obtained using standard finite element techniques. In this work, the element used is two-noded, with each node having 3 DOFs to describe the transverse displacement w and the bending θ and shear ϕ rotations [46]. Therefore, the element matrices $\mathbf{M}_b = [m_{ij}]$, $\mathbf{C}_b = [c_{ij}]$, and $\mathbf{K}_b = [k_{ij}]$ of the host beam alone are 6×6 dimensional while $\mathbf{U}_b = \begin{bmatrix} w_1 & \theta_1 & \phi_1 & w_2 & \theta_2 & \phi_2 \end{bmatrix}^T$ is a 6×1 column vector containing the generalized displacements of the host beam alone. Next, the previous element matrices can be augmented with one-set of the discretized equations derived in Sect. 2.3 to account for the presence of inerter resonators by including u_s and u_b as additional DOFs in the generalized displacements vector. For example, if a DC2 inerter resonator is attached to node 1 of a given element, then $M = m_{11}$, $u_s = w_1$, and $\mathbf{U}$ can be expanded in the following form:

$$\mathbf{U} = \begin{bmatrix} w_1 = u_s & \theta_1 & \phi_1 & w_2 & \theta_2 & \phi_2 & u_v & u_b \end{bmatrix}^T \tag{12}$$

while the corresponding matrices can be expressed as follows:

$$\mathbf{M} = \begin{bmatrix} m_{11} = M & m_{12} & m_{13} & m_{14} & m_{15} & m_{16} & 0 & 0 \\ m_{21} & m_{22} & m_{23} & m_{24} & m_{25} & m_{26} & 0 & 0 \\ m_{31} & m_{32} & m_{33} & m_{34} & m_{35} & m_{36} & 0 & 0 \\ m_{41} & m_{42} & m_{43} & m_{44} & m_{45} & m_{46} & 0 & 0 \\ m_{51} & m_{52} & m_{53} & m_{54} & m_{55} & m_{56} & 0 & 0 \\ m_{61} & m_{62} & m_{63} & m_{64} & m_{65} & m_{66} & 0 & 0 \\ 0 & 0 & 0 & 0 & 0 & 0 & m_v & 0 \\ 0 & 0 & 0 & 0 & 0 & 0 & 0 & b \end{bmatrix} \tag{13a}$$

$$\mathbf{C} = \begin{bmatrix} c_{11} + c_v & c_{12} & c_{13} & c_{14} & c_{15} & c_{16} & -(c_v + c_i) & c_i \\ c_{21} & c_{22} & c_{23} & c_{24} & c_{25} & c_{26} & 0 & 0 \\ c_{31} & c_{32} & c_{33} & c_{34} & c_{35} & c_{36} & 0 & 0 \\ c_{41} & c_{42} & c_{43} & c_{44} & c_{45} & c_{46} & 0 & 0 \\ c_{51} & c_{52} & c_{53} & c_{54} & c_{55} & c_{56} & 0 & 0 \\ c_{61} & c_{62} & c_{63} & c_{64} & c_{65} & c_{66} & 0 & 0 \\ -c_v & 0 & 0 & 0 & 0 & 0 & -(c_v + c_i) & -c_i \\ 0 & 0 & 0 & 0 & 0 & 0 & -c_i(1 + \frac{b}{m_{11}}) & c_i(1 + \frac{b}{m_{11}}) \end{bmatrix} \tag{13b}$$

$$\mathbf{K} = \begin{bmatrix} k_{11} + k_v & k_{12} & k_{13} & k_{14} & k_{15} & k_{16} & -(k_v + k_i) & k_i \\ k_{21} & k_{22} & k_{23} & k_{24} & k_{25} & k_{26} & 0 & 0 \\ k_{31} & k_{32} & k_{33} & k_{34} & k_{35} & k_{36} & 0 & 0 \\ k_{41} & k_{42} & k_{43} & k_{44} & k_{45} & k_{46} & 0 & 0 \\ k_{51} & k_{52} & k_{53} & k_{54} & k_{55} & k_{56} & 0 & 0 \\ k_{61} & k_{62} & k_{63} & k_{64} & k_{65} & k_{66} & 0 & 0 \\ -k_v & 0 & 0 & 0 & 0 & 0 & k_v + k_i & -k_i \\ \frac{b}{m_{11}}k_v & 0 & 0 & 0 & 0 & 0 & -\left[\frac{b}{m_{11}}(k_v + k_i) + k_i\right] & k_i(1 + \frac{b}{m_{11}}) \end{bmatrix} \tag{13c}$$

where Eq. (9) has been explicitly utilized to construct Eq. (13). Finally, we note that the matrices given in Eq. (13) can be particularly used for elements with resonator attachments, i.e., only for beam elements at appropriate locations along the beam length. For elements that are not attached to resonators, the 6×6 element matrices discussed earlier for a standard Timoshenko beam do not need further alterations. For completeness, the element matrices corresponding to DC1 and DC3 are provided in the "Appendix".

3 Mechanics of bandgap formation in inertant metamaterials

In this section, we investigate the effects of different design parameters on bandgap formation in inertant metamaterials in their undamped form. Following this analysis and building off of it, we will detail the metadamping phenomenon and its associated features in the context of dissipative inertant metamaterials in the next section. The mechanical system considered in this study consists of a cantilevered Aluminum Timoshenko beam which is $L = 360$ mm long, $W = 40$ mm wide, and $T = 6$ mm thick. The beam has a density of $\rho = 2,700$ kg/m^3 and a Young's modulus of 70 GPa. Twelve inerter resonators are periodically distributed over the beam's length, which implies that any two consecutive resonators are a distance $a = 30$ mm apart. The total mass of a single inerter resonator is kept constant at all times with $m_v + b = 0.4 m_b$, where $m_b = \rho W T a$ is the mass of the host beam portion contained in a single cell. The tuning frequency of the local resonators is $\omega_t = \sqrt{k_v / m_v}$. Finally, the non-dimensional parameters $\delta = (b/m_v)$ and $\phi = (\omega_c / \omega_t)$ are defined as the inertance and frequency ratios, respectively, where $\omega_c = \sqrt{k_i / b}$ is known as the corner frequency.

3.1 Bandgap formation in UC1

Bandgaps are characterized by their (1) width (i.e., frequency span) and (2) location along the frequency spectrum, and are commonly obtained via a dispersion analysis of a single unit cell. The emphasis here will be on scrutinizing bandgaps of the local resonance type regardless of the presence (or lack thereof) of Bragg bandgaps in any of these configurations. Figure 3a shows the band structure for a unit cell with UC1 as the mechanical network, plotting the dimensionless undamped frequency $\Omega_u = \frac{\omega_u}{\omega_t}$ versus the dimensionless wavenumber κa. The dashed-dotted acoustic (lower) and optical (upper) branches in Fig. 3a correspond to a zero inertance ratio ($\delta = 0$), which corresponds to a unit cell of a conventional metamaterial beam with an undamped classical resonator. The local resonance bandgap induced in this particular case spans the $0.996 - 1.183$ range on the vertical frequency axis. This is consistent with previous literature which has showed that locally resonant bandgaps start slightly below the tuning frequency ($\Omega_u = 1$) in conventional lumped elastic

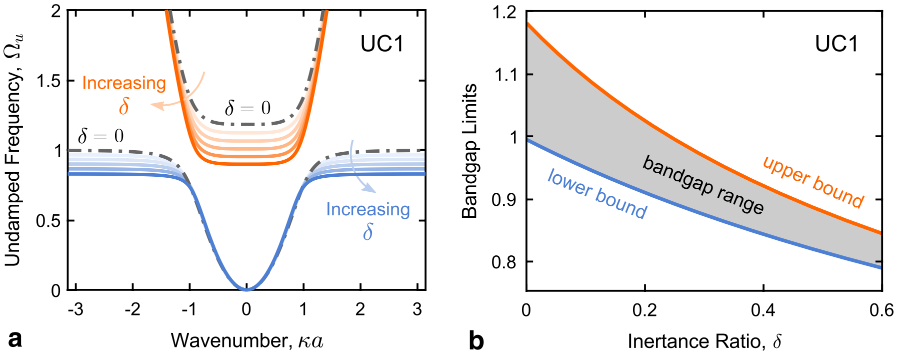

Fig. 3 Bandgap formation in undamped inertant metamaterials (UC1). **a** Band structure for a unit cell with UC1 as the mechanical network: the dashed-dotted lines correspond to a zero inertance ratio ($\delta = 0$) whereas the solid lines correspond to nonzero δ values. Darker lines depict larger δ values. The evolution of the bandgap limits corresponding to the unit cell in **a** is shown in **b** as function of δ

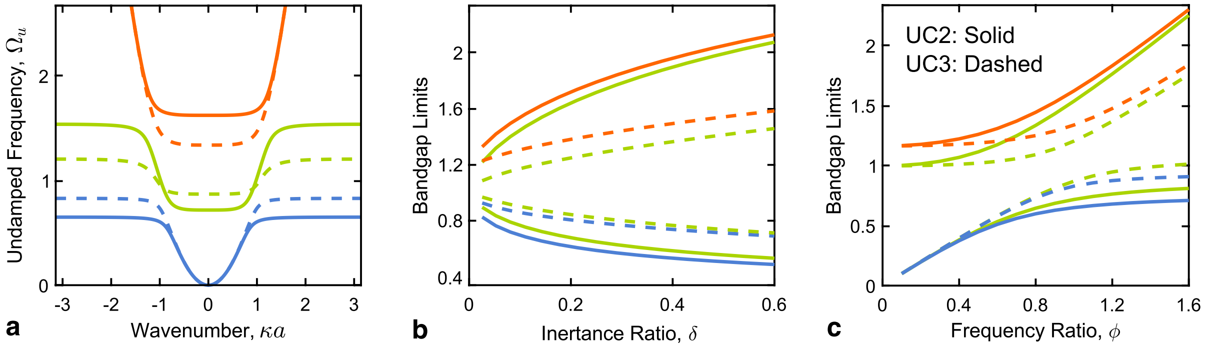

Fig. 4 Bandgap formation in undamped inertant metamaterials (UC2 and UC3). **a** A comparison between the band structures for two unit cells with UC2 (solid) and UC3 (dotted) as mechanical networks (for $\phi = 1$ and $\delta = \frac{1}{7}$). The evolution of the bandgap limits corresponding to the unit cells in **a** are shown in **b** as function of δ (when $\phi = 1$) and in **c** as function of ϕ (when $\delta = \frac{1}{7}$)

metamaterials [11]. The rest of the curves represent different UC1 unit cells with varying nonzero δ values. They are graded (light to dark) colors with the darker lines representing larger δ values. As can be seen, when δ increases, both the acoustic and optical branches are down-shifted as a result of inertial amplification and, as a consequence, induced bandgaps are shifted to lower frequency zones. This downshift in bandgap range is favorable for applications requiring suppression of elevated vibroacoustic amplitudes within low frequency regimes. However, this comes at the expense of bandgap width as shown Fig. 3b, which tracks the lower and upper bandgap bounds (and therefore width) with increasing inertance ratios.

3.2 Bandgap formation in UC2 and UC3

Figure 4 examines unit cells with UC2 and UC3 as mechanical networks. Since the inerter-spring arrangement in UC2 is reversed in UC3, these two configurations are analyzed simultaneously. Unlike UC1, these configurations produce two local resonance bandgaps as a result of an intermediate DOF. The band structures of both cells are shown in Fig. 4a for $\phi = 1$ and $\delta = \frac{1}{7}$, with the solid and dashed lines representing UC2 and UC3, respectively. The dispersion branches are color-coded similar to Fig. 3a (acoustic: blue; optical: orange), while the green lines represent the newly added intermediate branches. It is clear that each configuration is associated with its own dispersion properties, dictated by the widths and locations of its bandgaps which can be better understood by inspecting Fig. 4b, c. In Fig. 4b, bandgap limits are captured by sweeping along a sensible δ range with ϕ kept at 1. Two main observations are deduced from the figure: (1) Higher frequency bandgaps are wider than lower frequency ones over the considered δ range, in both UC2 and UC3 with the following caveat: UC2 gives rise to bandgaps that are closer to each other in terms of their widths whereas for UC3, the higher frequency bandgap is notably wider than the lower frequency one. (2) The frequency range separating both bandgaps increases proportionally with δ, in both UC2 and UC3. However, it remains wider in UC2 than in UC3 throughout the entire δ range. For example, when $\delta = \frac{1}{7}$, UC2 produces bandgaps that span the following frequency ranges: $0.649 - 0.717$ and $1.535 - 1.621$, while UC3 exhibits the following bandgaps: $0.828 - 0.953$ and $1.203 - 1.337$. This numerical example confirms both of the previous takeaways.

The evolution of bandgap limits as function of ϕ is shown in Fig. 4c, using $\delta = \frac{1}{7}$. It can be observed that as ϕ approaches zero, UC2 and UC3 produce a single bandgap that is identical in both cases as expected. However, a second low frequency bandgap starts to grow in size as ϕ increases. Furthermore, both bandgaps gradually shift to higher frequency regions as ϕ increases, with the lower frequency gap widening and the higher frequency one narrowing. Finally, a close look at the figure reveals that the frequency range separating both bandgaps reaches its smallest attainable value at $\phi = 0.6$ for UC2 and $\phi = 0.9$ for UC3.

4 Dissipation mechanics in inertant metamaterials

Augmented with damping, inertant metamaterials can bring about some unusual dispersion properties that are discussed in this section. Practically speaking, damping can potentially arise from both the host beam and the local inerter-based resonators. However, damping sources impact the overall dissipative behavior differently which is critical to note. We seek a better understanding of this by inspecting such damping sources separately in an attempt to isolate their individual effects on the emergent behavior. Since traditional (i.e., frequency-wavenumber) band structures were already presented, we focus here on the dissipative behavior which is most pertinent to this analysis and is best interpreted in the context of damping ratio vs. wavenumber and damping ratio vs. damped frequency band structures.

4.1 Damping in host beam only

We start by investigating the effect of utilizing a damped host beam of the inertant metamaterial. Given the lack of damping in any of the resonator components, our analysis remains focused on the undamped configurations (UC) of the mechanical networks. We adopt a proportional damping approach where $\mathbf{C}_b = \alpha \mathbf{K}_b$, with $\mathbf{C}_b$ and $\mathbf{K}_b$ denoting the viscous damping and stiffness matrices of the host beam. α is a proportionality constant that is selected to render $\zeta_b = 0.001$, where ζ_b is the fundamental mode's damping ratio. In the following, two inertant metamaterials composed of the same host beam but different resonator configurations (with UC2 and UC3 as mechanical networks) are compared, when $\phi = 1$ and $\delta = \frac{1}{7}$. The damping ratio band structures of both metamaterials are superimposed on top of each other in Fig. 5, with the solid and dotted lines being associated with UC2 and UC3, respectively. Figure 5a depicts the variation of Bloch damping ratios as function of wavenumbers, and is then used to obtain Fig. 5b which plots the damping ratio versus the dimensionless damped frequency $\Omega_d = \frac{\omega_d}{\omega_t}$. The latter enables unit cell predictions to be evaluated in the context of structural vibration rather than wave propagation since Bloch damping ratios are plotted against oscillatory frequencies in this case. We validate these results by computing the modal damping ratios of a finite beam with UC2 as mechanical network and plotting them as discrete points (circle markers) in Fig. 5b. These discrete points, which are in very close agreement with the solid curves at their respective locations, enable us to compare the realistic behavior of the finite metamaterial with the infinite medium predictions obtained from a single cell analysis. Three observations can be extracted from Fig. 5b as follows: (1) Bloch damping ratios exhibit vanishingly small values at the vicinity of bandgaps in both resonator configurations. (2) The intermediate branch exhibits a concave-down formation, irrespective of the used resonator configuration (However, the maximum attainable damping ratio in UC2 is higher than its counterpart corresponding to UC3). (3) Far away from the bandgap regions, the dissipative

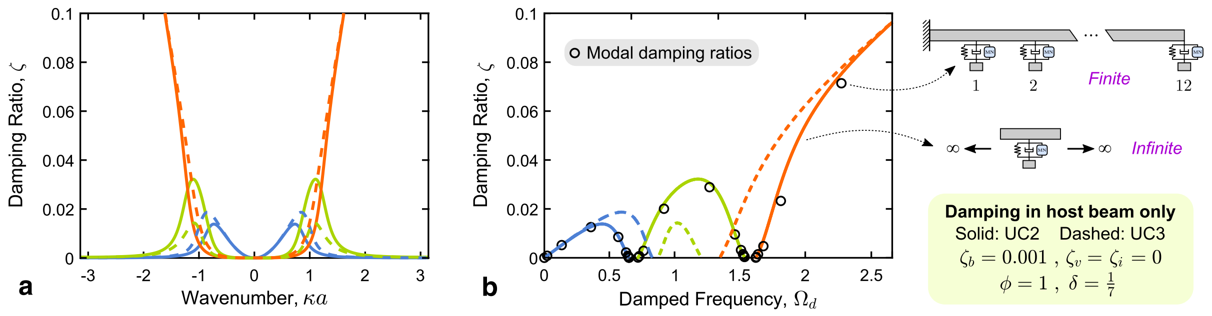

Fig. 5 Dissipative behavior of an inertant metamaterial beam with damping in the host beam only. A comparison between the **a** damping ratio and **b** damping-frequency band structures for two unit cells with UC2 (solid) and UC3 (dotted) as mechanical networks when $\zeta_b = 0.001$ while $\phi = 1$ and $\delta = \frac{1}{7}$. Damping in the resonator is ignored ($\zeta_v = \zeta_i = 0$). The modal damping ratios of a finite beam with UC2 as the mechanical network are plotted in **b** as discrete points (small black circles)

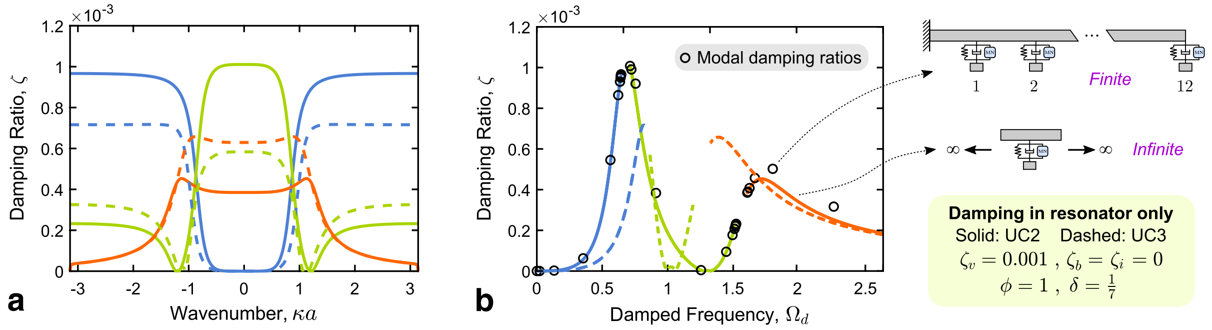

Fig. 6 Dissipative behavior of an inertant metamaterial beam with damping in the resonator only. A comparison between the **a** damping ratio and **b** damping-frequency band structures for two unit cells with UC2 (solid) and UC3 (dotted) as mechanical networks. Damping is placed outside the mechanical network component of the resonator only ($\zeta_v = 0.001$ and $\zeta_b = \zeta_i = 0$) while $\phi = 1$ and $\delta = \frac{1}{7}$. The modal damping ratios of a finite beam with UC2 as the mechanical network are plotted in **b** as discrete points (small black circles)

behavior of the acoustic and optical branches in both configurations is almost identical.

4.2 Damping in inerter resonator only

We now examine damping in the local resonators using an undamped host beam. While both viscous dampers c_v and c_i are resonator components, their influences on the overall dissipative behavior are radically different and therefore merit two separate investigations. In the first scenario, we look at an inertant metamaterial beam with $c_v \neq 0$ and $c_i = 0$ (i.e., damping placed outside the inerter-based mechanical network) and in the second, $c_v = 0$ and $c_i \neq 0$ (i.e., damping placed inside the inerter-based mechanical network).

4.2.1 Damping placement outside the mechanical network

Initially, the first scenario is examined for two inertant metamaterials composed of identical undamped host beams but different resonator configurations (with UC2 and UC3 as mechanical networks) when $\phi = 1$, $\delta = \frac{1}{7}$, and $\zeta_v = 0.001$. For both metamaterials, the damping ratio band structures are computed as shown in Fig. 6. The modal damping ratios associated with UC2 are calculated for a representative finite medium and superimposed on Fig. 6b for validation. We observe that: (1) The first bandgap is surrounded by Bloch damping ratios that are higher in UC2 than UC3 with the acoustic branch in UC2 being more dissipative than that of UC3. Conversely, Bloch damping ratios surrounding the second bandgap are higher in UC3 than UC2, especially at the start of the optical branch. (2) Both configurations exhibit extremely small damping ratios at some point along the intermediate branch which implies that as long as mechanical networks are rendered lossless, the resultant metamaterial will produce strongly oscillating vibration modes between induced bandgaps. Fortunately, damping placement inside the inerter-based mechanical network overcomes this problem, as will be shown next.

4.2.2 Damping placement inside the mechanical network

When $c_i \neq 0$, we need to shift our analysis to the three damped configurations DC1, DC2, and DC3. While each of these three configurations is comprised of an inerter, a spring, and a viscous damper, their respective arrangements and internal hierarchy has a significant effect on the emergent dispersion characteristics. As a case in point, the full dispersion properties for a unit cell with DC1 as mechanical network are comprehensively illustrated in Fig. 7. Interestingly, inerter resonators with this configuration produce only one local resonance bandgap (analogous to UC1) despite the presence of an additional DOF in their motion equations. This happens despite the presence of an intermediate branch as confirmed by Fig. 7, and mathematically anticipated given the additional DOF. Additionally, inertant metamaterials with

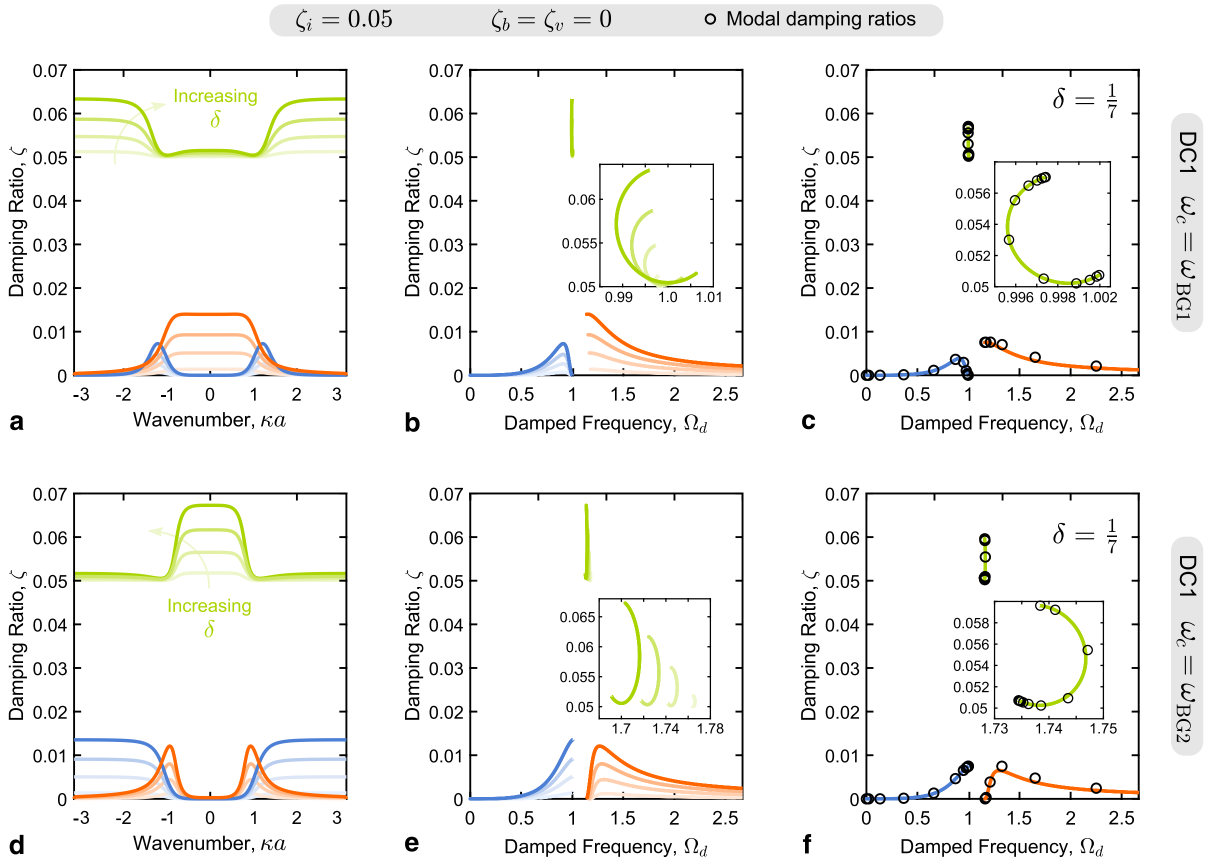

Fig. 7 Dissipative behavior of an inertant metamaterial beam with damping in the resonator only. Damping ratio and damping-frequency band structures for a unit cell with DC1 as the mechanical network. Damping is placed inside the mechanical network component of the resonator only ($\zeta_i = 0.05$ and $\zeta_b = \zeta_v = 0$). In **a**, **b**, the corner frequencies are tuned to $\omega_c = \omega_{\mathrm{BG1}}$ and in **d**, **e**, they are tuned to $\omega_c = \omega_{\mathrm{BG2}}$, using four different δ values (δ increases as the curves become darker). The results in **b**, **e** are validated in **c**, **f**, respectively, for the special case when $\delta = \frac{1}{7}$ by plotting the modal damping ratios of the corresponding finite mediums as discrete points (small black circles)

this configuration bring about some characteristics which depart from classical metamaterials. For example, Fig. 7a, b display the band structures for a DC1 unit cell corresponding to $\zeta_i = 0.05$ and four different inertance ratios (δ increases as the curves become darker). Each simulation depicts a δ value which is intentionally associated with a corner frequency that is tuned to $\omega_c = \omega_{\mathrm{BG1}}$, where ω_{BG1} is the frequency of the lower bound of the single local resonance bandgap present in this system. Figure 7d, e repeat the same exercise for a corner frequency tuned to the upper bandgap bound ($\omega_c = \omega_{\mathrm{BG2}}$). The four figures all show that the acoustic and optical branches can be shaped in different ways (as needed) by tuning the value of ω_c. When $\omega_c = \omega_{\mathrm{BG1}}$, the acoustic

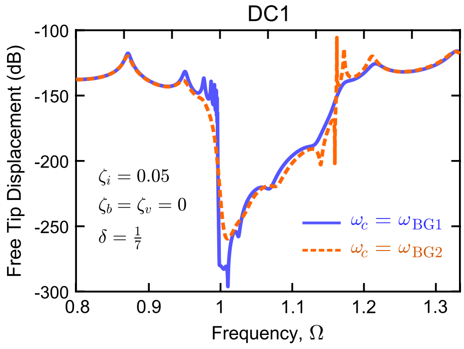

Fig. 8 Transverse displacements at the free tip of the cantilevered inertant metamaterial beams used in Fig. 7c ($\omega_c = \omega_{\mathrm{BG1}}$) and 7f ($\omega_c = \omega_{\mathrm{BG2}}$) with twelve resonators of DC1 as the mechanical network when an excitation force is applied a distance a from the fixed end of each beam

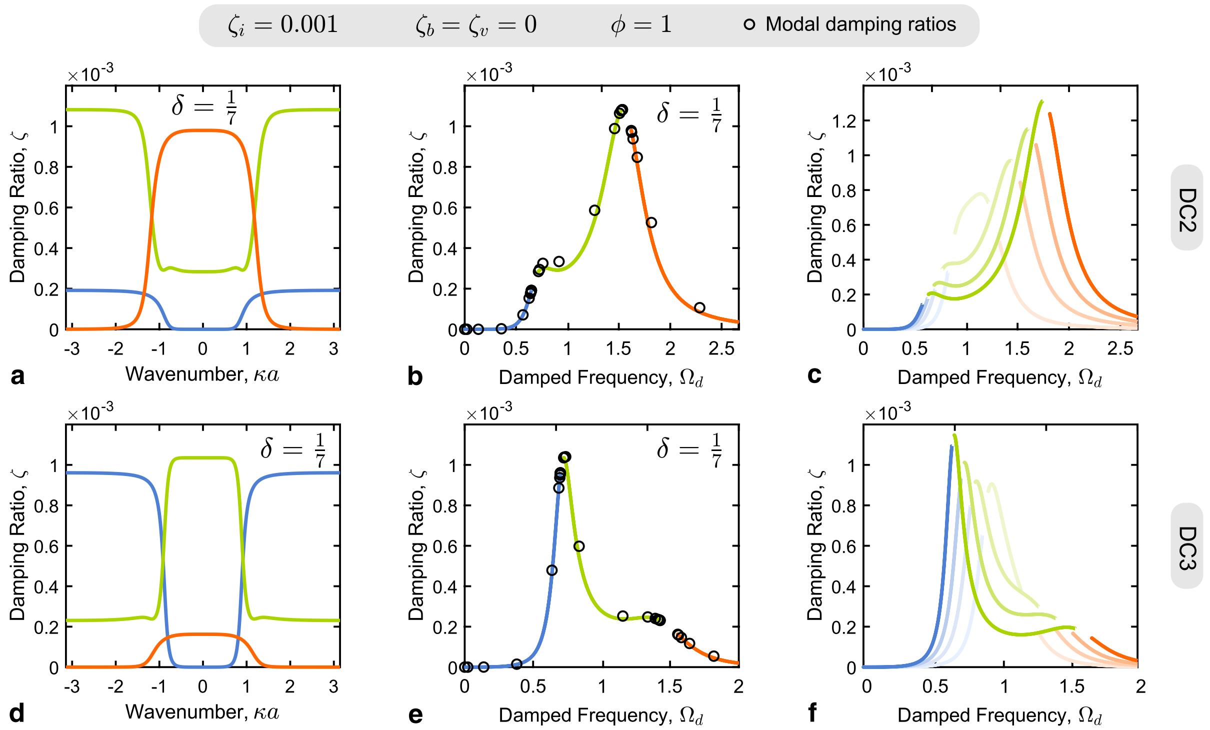

Fig. 9 Dissipative behavior of an inertant metamaterial beam with damping in the resonator only. Damping ratio and damping-frequency band structures for two unit cells with **a**, **c** DC2 and **d**, **f** DC3 as mechanical networks. Damping is placed inside the mechanical network component of the resonator only ($\zeta_i = 0.001$ and $\zeta_b = \zeta_v = 0$). The results in **a**, **b**, **d**, **e** are shown for the special case when $\phi = 1$ and $\delta = \frac{1}{7}$, which are validated in **b**, **e** by plotting the modal damping ratios of the corresponding finite mediums as discrete points (small black circles). **c**, **f** are computed using four different δ values (δ increases as the curves become darker)

branch is deliberately shaped to exhibit vanishingly small damping ratios at the bandgap's lower bound frequency and when $\omega_c = \omega_{\mathrm{BG2}}$, similar properties are achieved at the bandgap's upper bound frequency. Moreover, it is clear that the intermediate branch is always associated with relatively highly dissipative Bloch modes. This is found to be the case even for small ζ_i values. Finally, the results in Fig. 7b, e are validated in Fig. 7c, f, respectively, for the special case when $\delta = 1/7$ by plotting the modal damping ratios of the corresponding finite mediums. It is clear that the intermediate branches in both figures are realized by vibration modes inside the bandgaps (see close-up insets). Consequently, a critical question that arises from the previous discussion is whether these vibration modes are detrimental to the integrity of the bandgaps. A definite answer to this can be readily inferred from Fig. 8, which computes the transverse displacements at the tip points of the cantilevered inertant metamaterial beams used in Fig. 7c, f when a transverse excitation force is applied a distance a from the fixed end of each respective beam. The frequency response plot clearly shows that the bandgaps are not affected by the presence of such vibration modes within their bounds.

Finally, we show that efficient vibration damping between induced bandgaps can be achieved when DC2 or DC3 is utilized. To this end, Fig. 9 depicts their corresponding damping ratio and damping-frequency band structures when $\phi = 1$, $\zeta_v = 0$, and $\zeta_i = 0.001$. Unlike their earlier counterparts (with $\zeta_i = 0$, shown in Fig. 6), the intermediate branches in Fig. 9 (with Fig. 9a, b and d, e being associated with DC2 and DC3, respectively, when $\delta = \frac{1}{7}$) do not produce vanishingly small damping ratios, rendering these two damped configurations more suitable for applications that require vibration control between bandgaps. It is interesting to see how the dispersion branches evolve as function of the inertance ratio.

This is shown in Fig. 9c, f using four different δ values with graded (light to dark) colors where the darker ones are associated with larger δ values. For DC2 (Fig. 9c), it is clear that as δ increases, higher Bloch damping ratios are attained around the second bandgap, which also leads to increasingly more dissipative optical branches. Conversely, lesser dissipative behavior is observed around the first bandgap as a result of increasing δ. On the other hand, the dispersion mechanics corresponding to DC3 are shown in Fig. 9e, which reveals the exact opposite properties of DC2. More importantly, the intermediate branch in both DC2 and DC3 switch its concavity as a result of sweeping from smaller to larger δ values, changing it from concave-down to concave-up formation as can be inferred from Fig. 9c, f.

5 Conclusions

In this paper, a class of elastic metamaterials where an inerter element is integrated in a lumped mechanical network, which itself is a component of a locally resonant substructure, was thoroughly investigated. The layout of the mechanical network including the nature of its components, the precise location of the inerter within it, as well as the source of damping in the metamaterial were all shown to play central roles in shaping their dispersion mechanics and dissipative performance. Overall, six configurations of inerter resonators comprising different design architectures were examined: UC1 through UC3 as the undamped networks and DC1 through DC3 being their damped counterparts. In terms of bandgap characteristics, the following summarizes the two most important takeaways:

- When UC1 (or DC1) is used as the mechanical network, one local resonance bandgap is generated (despite the presence of an intermediate dispersion branch in the DC1 case). As the inertance ratio increases, the gap is down-shifted along the frequency axis at the expense of its width.
- UC2 and UC3 (as well as DC2 and DC3) each yields two bandgaps. Over a sensible range of inertance ratios, it is shown that:

    1. Higher frequency bandgaps are wider than lower frequency ones in both UC2 and UC3 with the following caveat: UC2 gives rise to bandgaps that are closer to each other in terms of their widths whereas for UC3, the higher frequency bandgap is significantly wider than the lower frequency one.
    2. The frequency range separating both bandgaps increases proportionally with the inertance ratio, in both UC2 and UC3.

Dissipation was shown to play a critical role in the design of inertant metamaterials. Unconventional band structures that directly relate Bloch damping ratios to oscillatory damped frequencies are implemented in the analysis. The mechanics of dissipation show that when DC1 is used, the acoustic and optical branches can be shaped in different ways (as needed) by tuning the corner frequency. Moreover, the presence of an intermediate branch is realized by vibration modes inside the bandgap. It was shown, however, that the aforementioned modes are not detrimental to the bandgap itself as evident from the frequency response of the finite realization. Following a similar analysis of both DC2 and DC3, it is observed that when damping is placed outside the inerter-based mechanical network, vanishingly small damping ratios appear at some point along the intermediate branch. The latter implies that as long as mechanical networks are rendered lossless, respective finite systems definitely produce strongly oscillating modes between the gaps. Fortunately, damping placement inside the inerter-based mechanical network overcomes this problem, enabling efficient broadband mitigation between the gaps. It was also shown that modal damping ratios obtained for a given finite inertant metamaterial beam enable a very efficient and direct comparison with unit cell predictions by providing discrete data points at their respective frequency locations, which can be superimposed on the aforementioned damping-frequency band structures. These modal damping ratios were shown to be in very close agreement with the dissipative dispersion mechanics predicted from the various damped configurations throughout the study. The work presented here provides a comprehensive framework for the analysis of complex and hierarchical mechanical networks which comprise arbitrary combinations of elastic, dissipative, and inerter elements, and that can be readily extended to different configurations; thus expanding the current design space of resonant metamaterials beyond the traditional notion of basic spring-mass absorbers. Most importantly, it sheds light on the interplay between prescribed damping and emergent dissipation in dispersive inertant structures;

effectively changing the current paradigm from one that merely looks at damping amount to a more effective placement-based strategy which selectively inserts a given (fixed) damping amount within the resonant network with the aim of maximizing the overall dissipative effect.

Acknowledgements M. Nouh acknowledges the support of this work from the US National Science Foundation through Award No. 1847254 (CAREER).

Declaration

Conflict of interest The authors declare that they have no conflict of interest.

Appendix

When DC2 is replaced with DC1 or DC3 in Fig. 2d, the resulting mass matrix is identical to Eq. (13a). However, the damping and stiffness matrices corresponding to DC1 can be expressed as follows:

$$\mathbf{C}=\begin{bmatrix} c_{11}+c_v+c_i & c_{12} & c_{13} & c_{14} & c_{15} & c_{16} & -c_v & -c_i \\ c_{21} & c_{22} & c_{23} & c_{24} & c_{25} & c_{26} & 0 & 0 \\ c_{31} & c_{32} & c_{33} & c_{34} & c_{35} & c_{36} & 0 & 0 \\ c_{41} & c_{42} & c_{43} & c_{44} & c_{45} & c_{46} & 0 & 0 \\ c_{51} & c_{52} & c_{53} & c_{54} & c_{55} & c_{56} & 0 & 0 \\ c_{61} & c_{62} & c_{63} & c_{64} & c_{65} & c_{66} & 0 & 0 \\ -(c_v+c_i) & 0 & 0 & 0 & 0 & 0 & c_v & c_i \\ -c_i(1+\frac{b}{m_v}) & 0 & 0 & 0 & 0 & 0 & 0 & c_i(1+\frac{b}{m_v}) \end{bmatrix} \tag{14}$$

and

$$\mathbf{K}=\begin{bmatrix} k_{11}+k_v & k_{12} & k_{13} & k_{14} & k_{15} & k_{16} & -k_v & 0 \\ k_{21} & k_{22} & k_{23} & k_{24} & k_{25} & k_{26} & 0 & 0 \\ k_{31} & k_{32} & k_{33} & k_{34} & k_{35} & k_{36} & 0 & 0 \\ k_{41} & k_{42} & k_{43} & k_{44} & k_{45} & k_{46} & 0 & 0 \\ k_{51} & k_{52} & k_{53} & k_{54} & k_{55} & k_{56} & 0 & 0 \\ k_{61} & k_{62} & k_{63} & k_{64} & k_{65} & k_{66} & 0 & 0 \\ -k_v & 0 & 0 & 0 & 0 & 0 & k_v & 0 \\ -(\frac{b}{m_v})k_v & 0 & 0 & 0 & 0 & 0 & \left[(\frac{b}{m_v})k_v-k_i\right] & k_i \end{bmatrix} \tag{15}$$

whereas the damping and stiffness matrices corresponding to DC3 can be written as:

$$\mathbf{C}=\begin{bmatrix} c_{11}+c_v & c_{12} & c_{13} & c_{14} & c_{15} & c_{16} & -c_v & 0 \\ c_{21} & c_{22} & c_{23} & c_{24} & c_{25} & c_{26} & 0 & 0 \\ c_{31} & c_{32} & c_{33} & c_{34} & c_{35} & c_{36} & 0 & 0 \\ c_{41} & c_{42} & c_{43} & c_{44} & c_{45} & c_{46} & 0 & 0 \\ c_{51} & c_{52} & c_{53} & c_{54} & c_{55} & c_{56} & 0 & 0 \\ c_{61} & c_{62} & c_{63} & c_{64} & c_{65} & c_{66} & 0 & 0 \\ -c_v & 0 & 0 & 0 & 0 & 0 & c_v & 0 \\ 0 & 0 & 0 & 0 & 0 & 0 & -c_i & c_i \end{bmatrix} \tag{16}$$

and

$$\mathbf{K}=\begin{bmatrix} k_{11}+k_v+k_i & k_{12} & k_{13} & k_{14} & k_{15} & k_{16} & -k_v & -k_i \\ k_{21} & k_{22} & k_{23} & k_{24} & k_{25} & k_{26} & 0 & 0 \\ k_{31} & k_{32} & k_{33} & k_{34} & k_{35} & k_{36} & 0 & 0 \\ k_{41} & k_{42} & k_{43} & k_{44} & k_{45} & k_{46} & 0 & 0 \\ k_{51} & k_{52} & k_{53} & k_{54} & k_{55} & k_{56} & 0 & 0 \\ k_{61} & k_{62} & k_{63} & k_{64} & k_{65} & k_{66} & 0 & 0 \\ -(k_v+k_i) & 0 & 0 & 0 & 0 & 0 & k_v & k_i \\ -\left[(\frac{b}{m_v})(k_v+k_i)+k_i\right] & 0 & 0 & 0 & 0 & 0 & (\frac{b}{m_v})k_v & k_i(1+\frac{b}{m_v}) \end{bmatrix} \tag{17}$$

References

1. Hagedorn P, Spelsberg-Korspeter G (2014) Active and passive vibration control of structures, vol. 558. Springer
2. Franchek M, Ryan M, Bernhard R (1996) Adaptive passive vibration control. J Sound Vib 189(5):565
3. Dalela S, Balaji P, Jena D (2021) A review on application of mechanical metamaterials for vibration control. Mech Adv Mater Struct 1–26
4. Nouh M, Aldraihem O, Baz A (2014) Vibration characteristics of metamaterial beams with periodic local resonances. J Vib Acoust 136(6):61012. https://doi.org/10.1115/1.4028453

5. Baravelli E, Ruzzene M (2013) Internally resonating lattices for bandgap generation and low-frequency vibration control. J Sound Vib 332(25):6562. https://doi.org/10.1016/j.jsv.2013.08.014
6. Al Ba'ba'a H, Attarzadeh M, Nouh M et al (2018) Experimental evaluation of structural intensity in 2D plate-type locally resonant elastic metamaterials. J Appl Mech 85(4):041005
7. Aladwani A, Almandeel A, Nouh M (2019) Fluid-structural coupling in metamaterial plates for vibration and noise mitigation in acoustic cavities. Int J Mech Sci 152:151
8. Bruggi M, Corigliano A (2019) Optimal 2D auxetic micro-structures with band gap. Meccanica 54(13):2001
9. Bacigalupo A, Gambarotta L, Lepidi M, Vadalà F (2019) Acoustic waveguide filters made up of rigid stacked materials with elastic joints. Meccanica 54(13):2039
10. Liu Z, Zhang X, Mao Y, Zhu Y, Yang Z, Chan CT, Sheng P (2000) Locally resonant sonic materials. Science 289(5485):1734
11. Al Ba'ba'a H, Nouh M, Singh T (2017) Formation of local resonance band gaps in finite acoustic metamaterials: a closed-form transfer function model. Sound Vib J 410:429
12. Huang H, Sun C (2009) Wave attenuation mechanism in an acoustic metamaterial with negative effective mass density. New J Phys 11(1):013003
13. Al Ba'ba'a H, Nouh M (2017) An investigation of vibrational power flow in one-dimensional dissipative phononic structures. J Vib Acoust 139(2):021003
14. Banerjee A (2020) Non-dimensional analysis of the elastic beam having periodic linear spring mass resonators. Meccanica 55(5):1181
15. Krushynska AO, Miniaci M, Kouznetsova VG, Geers MG (2017) Multilayered inclusions in locally resonant metamaterials: two-dimensional versus three-dimensional modeling. J Vib Acoust 139(2)
16. Nouh M, Aldraihem O, Baz A (2015) Wave propagation in metamaterial plates with periodic local resonances. J Sound Vib 341:53. https://doi.org/10.1016/j.jsv.2014.12.030
17. Hu Y, Guo Z, Ragonese A, Zhu T, Khuje S, Li C, Grossman JC, Zhou C, Nouh M, Ren S (2020) A 3D-printed molecular ferroelectric metamaterial. Proc Natl Acad Sci 117(44):27204
18. Sugino C, Leadenham S, Ruzzene M, Erturk A (2017) An investigation of electroelastic bandgap formation in locally resonant piezoelectric metastructures. Smart Mater Struct 26(5):055029
19. Callanan J, Willey C, Chen V, Liu J, Nouh M, Juhl A (2021) Uncovering low frequency band gaps in electrically resonant metamaterials through tuned dissipation and negative impedance conversion. Smart Mater Struct 31(1):015002
20. Al Ba'ba'a H, Callanan J, Nouh M, Singh T (2018) Band gap synthesis in elastic monatomic lattices via input shaping. Meccanica 53(11):3105
21. Yilmaz C, Hulbert GM, Kikuchi N (2007) Phononic band gaps induced by inertial amplification in periodic media. Phys Rev B 76(5):054309
22. Yilmaz C, Hulbert G (2010) Theory of phononic gaps induced by inertial amplification in finite structures. Phys Lett A 374(34):3576
23. Acar G, Yilmaz C (2013) Experimental and numerical evidence for the existence of wide and deep phononic gaps induced by inertial amplification in two-dimensional solid structures. J Sound Vib 332(24):6389
24. Taniker S, Yilmaz C (2017) Generating ultra wide vibration stop bands by a novel inertial amplification mechanism topology with flexure hinges. Int J Solids Struct 106:129
25. Yuksel O, Yilmaz C (2020) Realization of an ultrawide stop band in a 2-D elastic metamaterial with topologically optimized inertial amplification mechanisms. Int J Solids Struct 203:138
26. Miniaci M, Mazzotti M, Amendola A, Fraternali F (2021) Effect of prestress on phononic band gaps induced by inertial amplification. Int J Solids Struct
27. Smith MC (2002) Synthesis of mechanical networks: the inerter. IEEE Trans Autom Control 47(10):1648
28. Chen MZ, Papageorgiou C, Scheibe F, Wang FC, Smith MC (2009) The missing mechanical circuit element. IEEE Circuits Syst Mag 9(1):10
29. Papageorgiou C, Houghton NE, Smith MC (2009) Experimental testing and analysis of inerter devices. J Dyn Syst Meas Control 131(1)
30. Wang FC, Hong MF, Lin TC (2011) Designing and testing a hydraulic inerter. Proc Inst Mech Eng C J Mech Eng Sci 225(1):66
31. Zhang R, Zhao Z, Pan C (2018) Influence of mechanical layout of inerter systems on seismic mitigation of storage tanks. Soil Dyn Earthq Eng 114:639
32. John ED, Wagg DJ (2019) Design and testing of a frictionless mechanical inerter device using living-hinges. J Franklin Inst 356(14):7650
33. Kulkarni PP, Manimala JM (2016) Longitudinal elastic wave propagation characteristics of inertant acoustic metamaterials. J Appl Phys 119(24):245101
34. Al Ba'ba'a H, DePauw D, Singh T, Nouh M (2018) Dispersion transitions and pole-zero characteristics of finite inertially amplified acoustic metamaterials. J Appl Phys 123(10):105106
35. Frandsen NM, Bilal OR, Jensen JS, Hussein MI (2016) Inertial amplification of continuous structures: large band gaps from small masses. J Appl Phys 119(12):124902
36. Fang X, Chuang KC, Jin X, Huang Z (2018) Band-gap properties of elastic metamaterials with inerter-based dynamic vibration absorbers. J Appl Mech 85(7)
37. Fang X, Chuang K.C, Jin X.L, Wang D.F, Huang ZL (2021) An inertant elastic metamaterial plate with extra wide low-frequency flexural band gaps. J Appl Mech 88(2)
38. Zeighami F, Palermo A, Marzani A (2019) Inertial amplified resonators for tunable metasurfaces. Meccanica 54(13):2053
39. Chowdhury S, Banerjee A, Adhikari S (2021) Structures, vol 33. Elsevier, pp 1340–1353
40. Banerjee A, Adhikari S, Hussein MI (2021) Inertial amplification band-gap generation by coupling a levered mass with a locally resonant mass. Int J Mech Sci 207:106630

41. Hussein MI, Frazier MJ (2013) Metadamping: an emergent phenomenon in dissipative metamaterials. J Sound Vib 332(20):4767
42. Frazier MJ, Hussein MI (2015) Viscous-to-viscoelastic transition in phononic crystal and metamaterial band structures. J Acoust Soc Am 138(5):3169
43. DePauw D, Al Ba'ba'a H, Nouh M (2018) Metadamping and energy dissipation enhancement via hybrid phononic resonators. Extreme Mech Lett 18:36
44. Bacquet CL, Al Ba'ba'a H, Frazier MJ, Nouh M, Hussein MI (2018) Chapter two-metadamping: dissipation emergence in elastic metamaterials. Adv Appl Mech 51:115
45. Aladwani A, Nouh M (2020) Mechanics of metadamping in flexural dissipative metamaterials: analysis and design in frequency and time domains. Int J Mech Sci 173:105459
46. Aladwani A, Nouh M (2021) Strategic damping placement in viscoelastic bandgap structures: dissecting the metadamping phenomenon in multiresonator metamaterials. J Appl Mech 88(2)
47. Hu Y, Chen MZ (2015) Performance evaluation for inerter-based dynamic vibration absorbers. Int J Mech Sci 99:297